(Supporting Information)

Colloidal Assembly by Directional Ice Templating

Bipul Biswas[1,2], Mayank Misra[3], Anil Singh Bisht[1], Sanat K. Kumar*[3]
Guruswamy Kumaraswamy*[1,4]

[1]Complex Fluid and Polymer Engineering, Polymer Science and Engineering, CSIR-National Chemical Laboratory, Dr. Homi Bhabha Road, Pune – 411008, India

[2]Academy of Scientific and Innovative Research (AcSIR), Ghaziabad-201002, India

[3] Department of Chemical Engineering, Columbia University, 500 West 120th Street, New York, New York 10027

[4]Current Address: Chemical Engineering Department, Indian Institute of Technology, Bombay, Powai-700076, India

1 Experimental

1.1 Visualizing ice crystal geometry during directional ice templating

We use an indirect method to visualize the size, shape and orientation of ice crystals during ice templating. We increase the amount of polymer and crosslinker added (total polymer concentration ~5%) and perform directional ice-templating using the protocol described in the main text. Use of a higher quantity of polymer and crosslinker results in the formation of a self-standing macro-porous scaffold.[1] The pores in the scaffold represent a negative replica of the ice crystals. Thus, quantifying the number density, shape and orientation of the pores in the scaffold gives us insights into the ice crystals that templated them. For scaffolds prepared using directional ice templating, we observe the formation of elongated pores oriented along the axis of the sample, viz. along the direction of propagation of the freezing front. The width of these pores is, on average ≈ 30 μm. An SEM image of the porous scaffolds prepared using directional ice templating is shown in Figure S 1A. We note that we do not observe any height dependence to the pore size (that results from the ice crystal template) along the temperature gradient direction. We have performed detailed studies where we have sectioned the samples and looked

for variations in particles with height. These experiments were done at low colloid concentrations but with sufficient polymer to trap the colloidal particles in crosslinked mesh. We sectioned the monolith as a function of height, took images and counted the number of particles. We find no evidence for systematic variation of particle concentration with height. Similarly, we also prepared scaffolds prepared using isotropic freezing and present a SEM image for the resultant scaffold in Figure S 1B.

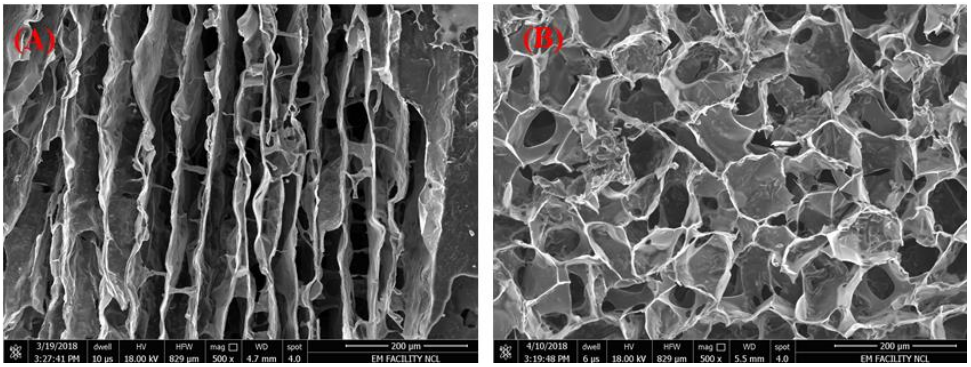

Figure S 1: SEM image of scaffold made with excess amount of polymer using (A) directional ice-templating and (B) isotropic ice templating. The voids represent a negative replica of the ice crystal templates.

1.2 Cluster identification and cluster size distributions using ImageJ

We use ImageJ to identify clusters and to characterize them. Raw data obtained from microscopy is imported into ImageJ and the background is subtracted using a "rolling ball algorithm" with a radius of 50 pixels.[2,3] Here, we determine a suitable background value for each pixel by averaging over a circle (here, with radius = 50 pixels) around the pixel. This background is then subtracted from the image to eliminate large spatial variation in background intensity. Subsequently, we convert the images into 8-bit binary format and finally threshold them to identify clusters. Clusters are identified and characterized using the "Analyze Particles" inbuilt routine in ImageJ. This routine employs an edge-detection algorithm to identify particles in an image. The process that we employ is similar to that reported in the literature[4,5] and is widely used to obtain the area and perimeter of clusters. We divide the cluster area by the area of a single particle (obtained by averaging over a large number of images) to obtain the number of particles in a cluster, n. n is obtained as the closest integer value to the area ratio. We estimate the error in the calculated value of n obtained by applying this protocol to a large number of isolated clusters by comparing the calculated value with a visual count of the number of

colloids (n) in the clusters. The error varies with the size of the cluster: we observe no error for clusters with $n \leq 5$; variations of ± 1 in about 20% of the images for $n \leq 15$ and variations of ± 2 in about 5% of the images for $20 \leq n \leq 30$.

We define a cluster when $n \geq 3$ colloids are identified to be connected, as explained below. We present data for clusters comprising ≥ 3 connected particles due to difficulties in quantifying the error in our estimates for $n = 1$ and $n = 2$. There are two sources for this error: (i) we count clusters by sedimenting them on a slide and observing these under a microscope. With increase in n, clusters sediment more readily. Particularly, for monomers (and to some extent for dimers), our experimental estimates likely represent an undercount. (ii) we observe a few instances of dimer colloidal clusters in the original colloidal suspension, even after thorough sonication. Therefore, we only report data for clusters comprising 3 or more particles. To improve the statistics for presentation, the cluster size data is presented after binning (with a bin size of 2). Therefore, for example, the data for for $n = 3$ and $n = 4$ clusters is binned together and is presented with the ordinate = 3.5.

Particle connectivity is determined by the thresholding employed when we use the "Analyze Particles" routine in ImageJ. Let us consider, for example, Figure S 2 (the third image from the left on the bottom of Figure 1). The threshold that we use in the manuscript counts this as one large connected cluster with a "tail" comprising four individual particles that are not part of this cluster (Figure S 3 a). To demonstrate that the cluster distributions obtained are robust to the choice of threshold, we re-analyze our data by changing the threshold to a sufficiently low value so that all the particles in the image form a single cluster (Figure S 3 b). For reference, we note that in our 8 bit images, pixel intensity varies from 0 to 255. After background subtraction, pixel intensities show a binary distribution: 0-10 for the background and 100-255 for the particles. The threshold was originally set at 100, and to re-analyze the data, we drastically lower this to 54. Even with this change, we observe that there is very little change in the cluster size distribution. For both thresholds, we obtain a power law distribution, with slopes of 2.10 ± 0.11, 2.48 ± 0.12 and 3.03 ± 0.27 for volume concentrations of $\varphi = 5 \times 10^{-2}$, 1.2×10^{-2} and 2.5×10^{-3}, respectively for the low threshold, as compared with 2.16 ± 0.16, 2.37 ± 0.18 and 3.16 ± 0.19 for the original threshold. The selection of threshold to determine which particle is in a cluster is arbitrary, especially in the case of some images. However, we demonstrate that the contribution from such images (as Figure S 3) is sufficiently small that our protocol for obtaining the cluster size distribution is robust even to drastic change in threshold selection.

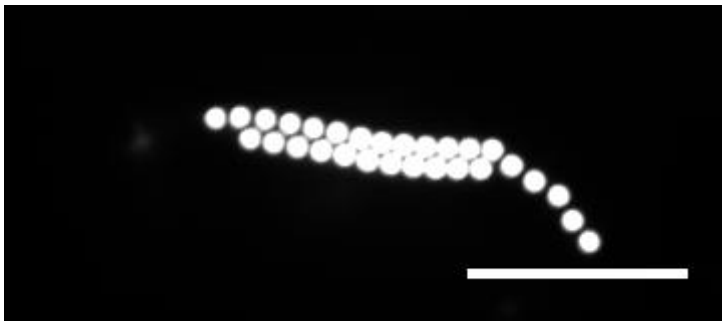

Figure S 2: Image of cluster used to exemplify analysis. The scale bar is 10 µm.

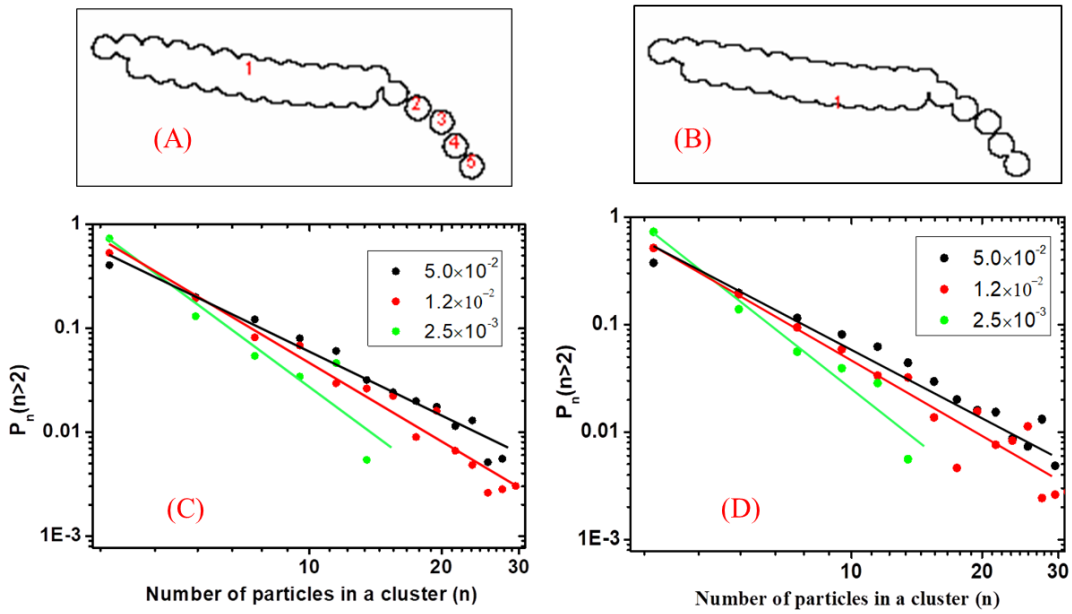

Figure S 3: (A) Cluster identification based on the original threshold value (100) in the manuscript. (B) Cluster identification using a very low value for the threshold (54). (C) Cluster size distribution based on the threshold in (A). (D) Cluster size distribution based on the threshold in (B).

Figure S 4: Determining the area and perimeter of a cluster.

To exemplify the process by which the perimeter and area are calculated, we consider the cluster in Figure S 4. We use the ImageJ protocol detailed earlier in this section to identify the cluster. In the methodology employed, the area obtained (A) for the cluster captures the edges of the particles that form the outer layer of the cluster as can be observed from Figure S 4. Therefore, the perimeters obtain (P) is the perimeter outer boundary of the cluster while the area is in the entire internal area included within this perimeter. We calculate $C = A/P^2$ and term this the connectivity of the cluster. The value of C is arbitrary, and correlates with the geometry of the clusters formed (2D planar assemblies versus linear string-like clusters).

1.3 Fraction of monomers and dimers

At low colloid concentration ($\varphi \sim 2.5 \times 10^{-3}$), most particles do not form clusters and remain as isolated particles or as dimers. At these concentrations, there are very few short linear chains, tapes or planar aggregates. With increase in particle concentration from $\varphi \sim 2.5 \times 10^{-3}$ to $\varphi = 5.0 \times 10^{-2}$, we observe the formation of long linear structures (comprising over 25 colloids) as well as more extended two-particle wide tapes and large planar structures. We note that, at lower concentration ($\varphi \sim 2.5 \times 10^{-3}$), nearly 80% of the particles exist as monomers or dimers. This reduces, approximately logarithmically with concentration, decreasing to 45% at a concentration of $\varphi = 5.0 \times 10^{-2}$ (Figure S 5). This trend is qualitatively similar to the case of ice templating by isotropic freezing.

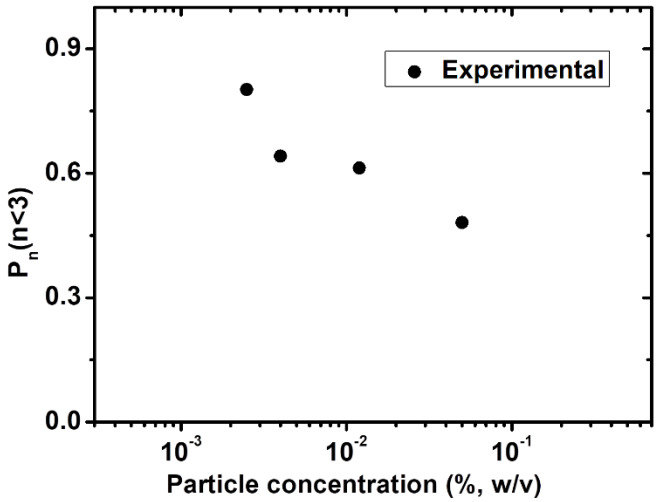

Figure S 5: Fraction of particles that exist as monomers or dimers. With the increasing particle concentration the number of existing monomers and dimers decrease (approximately logarithmically).

1.4 Cluster size distributions and data analysis

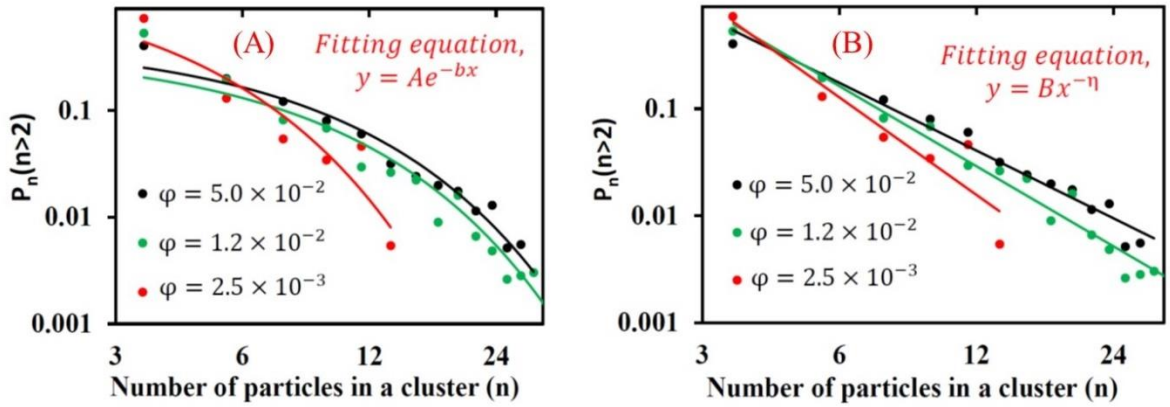

Figure S 6: (A) Cluster data fitting with exponential. (B) Cluster data fitting with power law.

Table 1: R^2 values of power fit and exponential fitting

Concentration of particles	$R^2 - Power$	$R^2 - exponential$
5.0×10^{-2}	*0.96*	*0.95*
1.2×10^{-2}	*0.94*	*0.90*
2.5×10^{-3}	*0.96*	*0.93*

Cluster size distributions are obtained after counting images containing at least 15000 particles (for the lowest concentrations) and at least 130000 particles at the highest concentration. We attempted to fit the data to different forms. We present fits to the data using exponential and power law forms (Figure S 6). The R^2 value for the power law fit is slightly better than that for the exponential fit. Also, visually, it is clear that the exponential fit does not capture the data at low n. Therefore, it is clear that the power law form provides a better representation of the data compared to an exponential fit. We note that we have data that extends a little over a decade in n. Data at large values of n exhibit poorer statistics since relatively few large clusters are obtained. Power law distributions are commonly observed in clustering processes. In our simulations, we invoke a simple model for clustering that reproduces the features from our experiments. Here too, the cluster size distribution is well-fitted to a power law form.

1.5 Connectivity

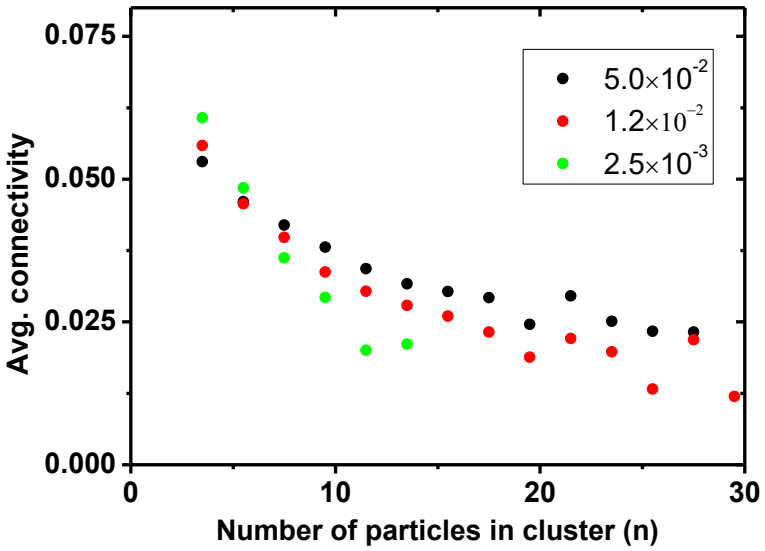

Figure S 7: Variation of avg. connectivity with cluster size.

We analyse how the shape of the particle clusters change with particle concentration. We define connectivity for a cluster as the ratio of the area of the cluster to the square of the cluster perimeter, viz C= (Area)/(Perimeter)^2, a dimensionless number. For a cluster with the same number of particles, an increased value of C indicates a transition in shape from a linear structure to a more isotropic shape. We estimate the average connectivity at a particular concentration and plot as a function of cluster size for different concentrations. We observe that the average value of C is higher at higher particle concentration (Figure S 7), which indicates the formation of isotropic planar clusters at higher concentration. We note that for larger clusters (viz. n > 10), there is an increase of average C with concentration.

2 Simulations:

2.1 Cluster formation from directional ice templating of colloidal dispersions

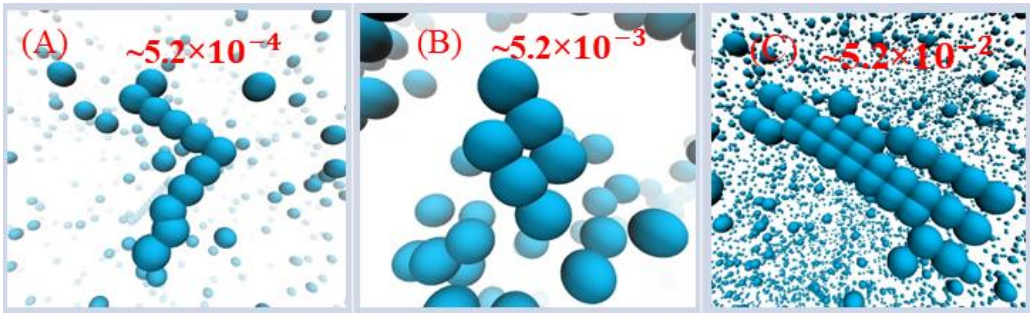

Figure S 8: Representative snapshots of the final particle configurations from directional ice templating simulations at particle concentrations of (A) $\varphi \sim 5.2 \times 10^{-4}$ *(B)* $\varphi \sim 5.2 \times 10^{-3}$ *(C)* $\varphi \sim 5.2 \times 10^{-2}$. *For ease of visualization, the ice crystals are not shown in the images.*

2.2 Fraction of monomers and dimers

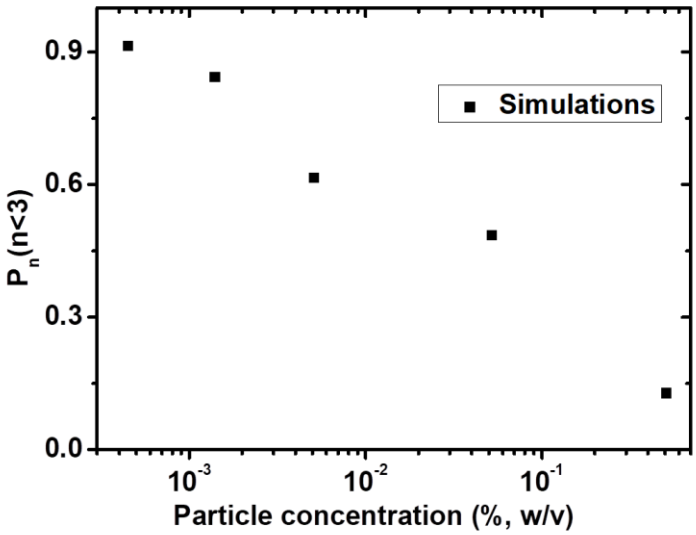

Figure S 9: Fraction of particles existing as monomers or dimers in simulations of directional ice-templating.

2.3 Connectivity

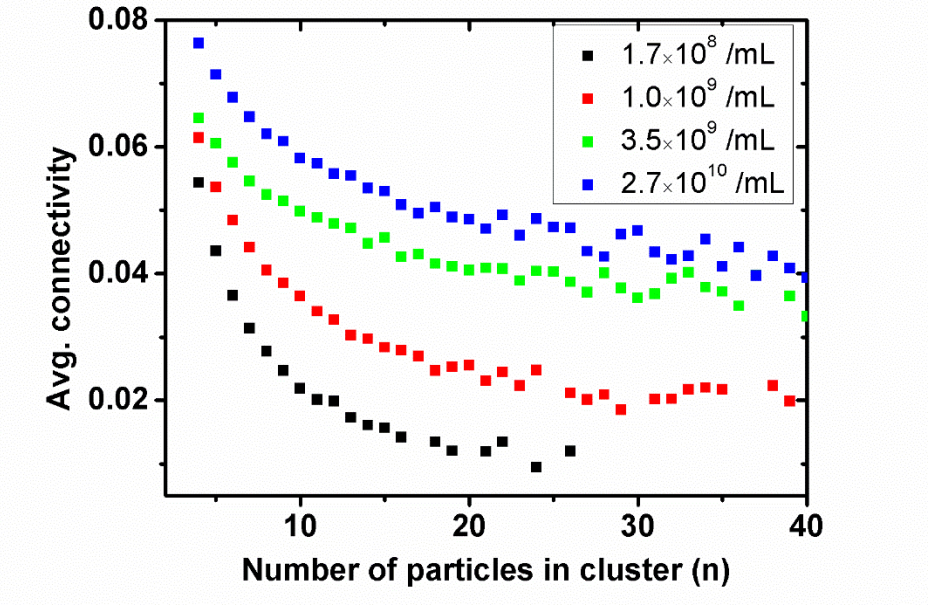

Figure S 10: Variation in the average connectivity with particle concentration.

Similar to the experiment, here also we analyse how the shape of the particle clusters change with particle concentration. We define connectivity for a cluster as the ratio of the area of the cluster to the square of the cluster perimeter, viz C= (Area)/(Perimeter)^2, a dimensionless number.

2.4 Definition of voids

2.4.1 Isotropic freezing:

Lattice points surrounded by ice crystals are identified as a void. Voids can be both inner voids (void 1 in left panel Figure S 11) or outer voids (void 2 in left panel Figure S 11).

1.1.1 Directional freezing:

As the ice crystals grow vertically from the lower surface, the freezing front height grows with time. We define voids only in the region of the sample below the top surface of the ice crystals at each time step. Similar to isotropic cooling we define a void as lattice points surrounded by ice crystals (right panel Figure S 11).

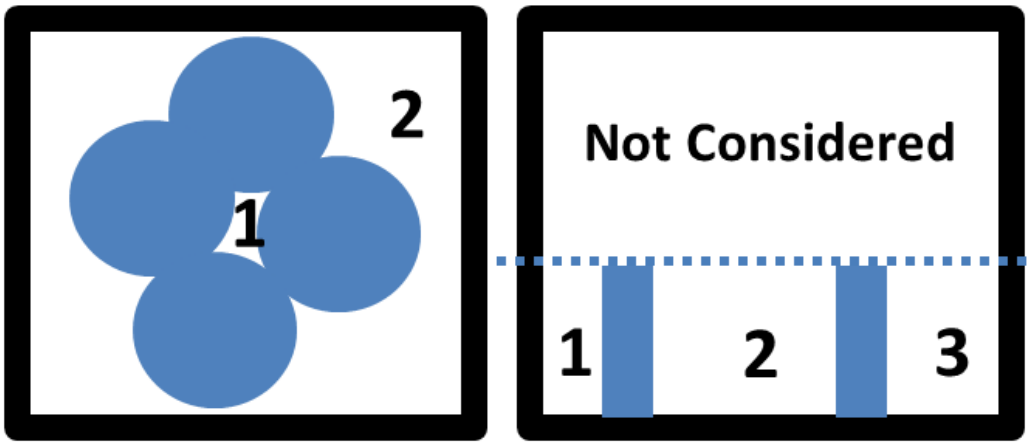

Figure S 11: Schematic representation of voids for (left) isotropic and (right) directional freezing simulations.

2.5 Determination of average ice crystal size

We note that the size and shape of the ice crystals in isotropic and directional freezing are different. The nucleation densities of ice crystals in our simulations is set to match that observed in our experiments. We select the nucleation density such that for isotropic freezing, the mean diameter of the ice crystal at impingement is ~50 µm and for directional ice templating, the width of a distorted rectangular ice crystal is ~30 µm. In **Error! Reference source not found.**A we show the variation of the number of voids in the simulation box with ice crystal growth. As ice crystals are nucleated and grow, the number of voids increases. For isotropic freezing, the number of voids reaches a maximum when the average size of the ice crystals is ~34.5 µm. Subsequently, as the ice crystals impinge, voids close up and the number of voids decreases. At the end of the simulation, when the box is filled with ice crystals, there are no voids. For directional cooling, ice seeds are randomly placed at the lower surface of the box and grow uniformly in X, Y and Z-direction. Here, we observe that the number of voids reaches a maximum value when the ice crystal thickness is 15 µm. Similar to the case of isotropic freezing, the number of voids subsequently decreases and approaches zero when the simulation box is filled with ice. In the simulations, we use the average size of the ice crystals as a proxy for the freezing time. The time for complete freezing is obtained as the time for the number of voids in the simulation box to go to zero. Getting completely filled lattices exactly at the maximum size of ice crystal is not always possible due to the randomness associated with starting state (placement of ice seeds and particles) of the simulations. We continue running simulations so ice grows into the void spaces until the simulation box is full. When the simulation is run 500 times, we find that when the simulation box is filled, the ice crystal size

ranges from 41 µm to 50 µm for isotropic freezing and 25 µm to 30 µm for directional freezing. Thus, we assume freezing is complete for directional growth when the ice crystal size is 27 µm and 45 µm for isotropic freezing. We define a non-dimensional freezing time, t_{ICE} as the ratio of the average ice crystal size to the ice crystal size when the voids close up as ice crystals impinge, viz. 27 µm for directional freezing and 45 µm for isotropic freezing. In **Error! Reference source not found.**B we present data for the fraction of the simulation box that is filled with voids, as a function of t_{ICE}.

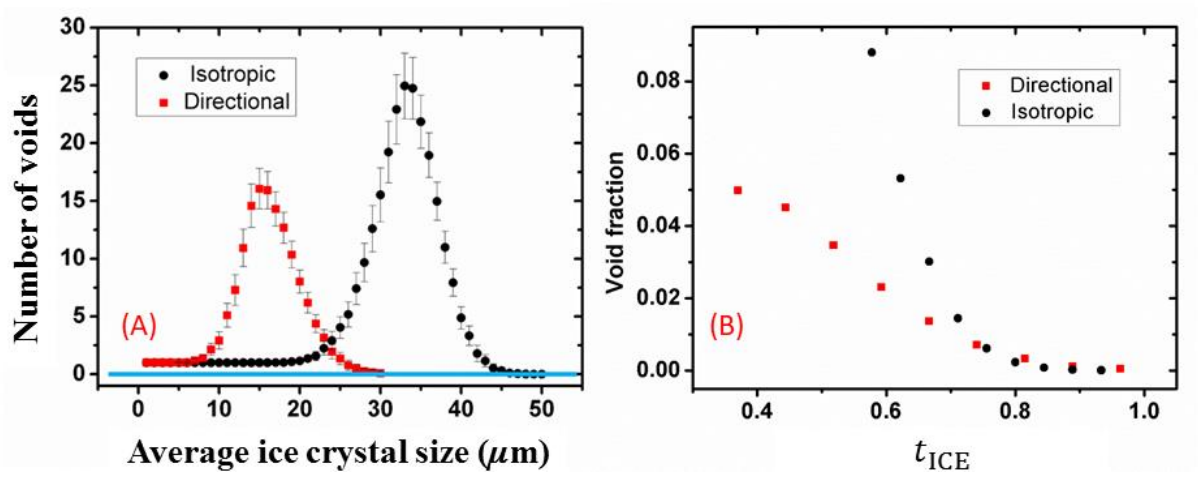

Figure S 12: The number of voids in the simulation box as a function of ice crystal size as freezing proceeds. The number of voids increases as the ice crystals grows and reaches a maximum at ~15 µm for directional and ~34.5 µm for isotropic freezing. The error bars represent the standard deviation from multiple simulation runs. (B) Variation of void fraction with respect to the simulation box as a function of ice crystal growth fraction (here both box sizes for isotropic and directional are same).

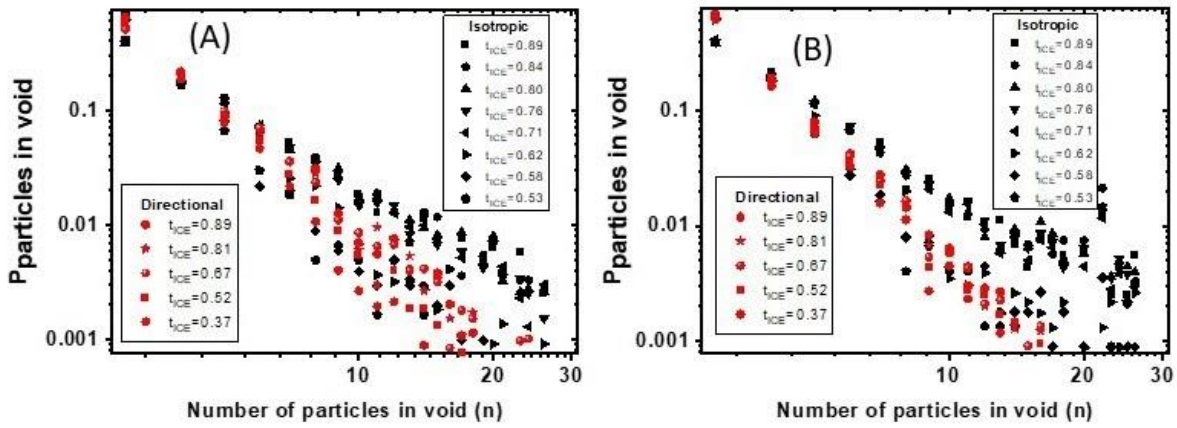

Figure S 13: Red symbols represent data for directional templating while black symbols are from isotropic ice templating. (A) In both the directional and isotropic processes, the particle concentration φ=6.8×10-3. (B) Particle concentration is φ=1.6×10-3.

2.6 Cluster size distribution when ice templating is done by liquid nitrogen

In Figure S 14, we present cluster size distribution obtained by ice templating when a colloidal dispersion is frozen isotropically by plunging the vial containing it into liquid nitrogen.

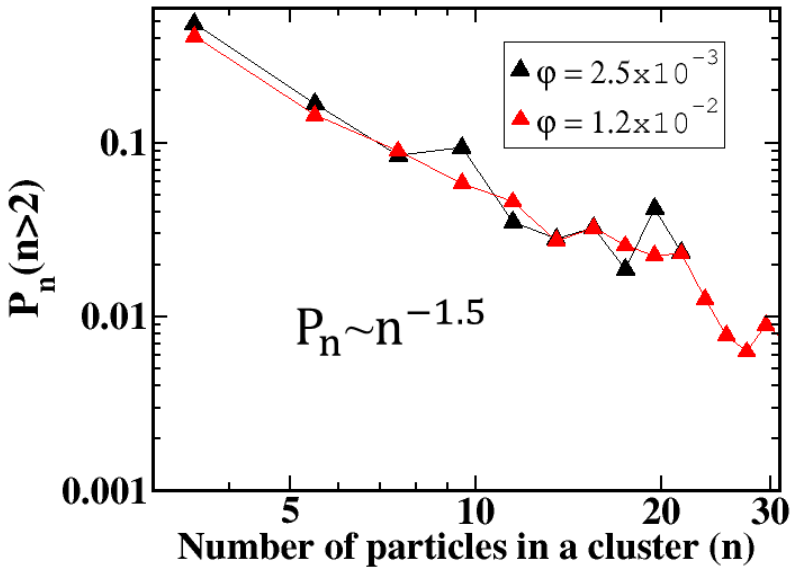

Figure S 14: Cluster size distribution obtained by ice templating when a colloidal dispersion is frozen isotropically by plunging the vial containing it into liquid nitrogen. Under these experimental conditions, the average ice crystal size in the bulk is ≈ 25 μm.

3 References:

1. Rajamanickam, R. *et al.* Soft colloidal scaffolds capable of elastic recovery after large compressive strains. *Chem. Mater.* **26**, 5161–5168 (2014).
2. Papadopulos, F. *et al.* Common tasks in microscopic and ultrastructural image analysis using ImageJ. *Ultrastruct. Pathol.* **31**, 401–407 (2007).
3. Baviskar, S. N. A quick & automated method for measuring cell area using ImageJ. *Am. Biol. Teach.* **73**, 554–556 (2011).
4. Baviskar, S. N. A quick & automated method for measuring cell area using ImageJ. *Am. Biol. Teach.* **73**, 554–556 (2011).
5. Papadopulos, F. *et al.* Common tasks in microscopic and ultrastructural image analysis using ImageJ. *Ultrastruct. Pathol.* **31**, 401–407 (2007).